HHS Public Access

Author manuscript

Magn Reson Med. Author manuscript; available in PMC 2016 March 01.

Published in final edited form as:

Magn Reson Med. 2008 November ; 60(5): 1135–1146. doi:10.1002/mrm.21740.

Respiratory Motion-Compensated Radial Dynamic Contrast-Enhanced (DCE)-MRI of Chest and Abdominal Lesions

Wei Lin[*], **Junyu Guo**, **Mark A. Rosen**, and **Hee Kwon Song**

Department of Radiology, University of Pennsylvania Medical Center, Philadelphia, Pennsylvania, USA

Abstract

Dynamic contrast-enhanced (DCE)-MRI is becoming an increasingly important tool for evaluating tumor vascularity and assessing the effectiveness of emerging antiangiogenic and antivascular agents. In chest and abdominal regions, however, respiratory motion can seriously degrade the achievable image quality in DCE-MRI studies. The purpose of this work is to develop a respiratory motion-compensated DCE-MRI technique that combines the self-gating properties of radial imaging with the reconstruction flexibility afforded by the golden-angle view-order strategy. Following radial data acquisition, the signal at *k*-space center is first used to determine the respiratory cycle, and consecutive views during the expiratory phase of each respiratory period (34–55 views, depending on the breathing rate) are grouped into individual segments. Residual intra-segment translation of lesion is subsequently compensated for by an autofocusing technique that optimizes image entropy, while intersegment translation (among different respiratory cycles) is corrected using 3D image correlation. The resulting motion-compensated, undersampled dynamic image series is then processed to reduce image streaking and to enhance the signal-to-noise ratio (SNR) prior to perfusion analysis, using either the *k*-space-weighted image contrast (KWIC) radial filtering technique or principal component analysis (PCA). The proposed data acquisition scheme also allows for high framerate arterial input function (AIF) sampling and free-breathing baseline T_1 mapping. The performance of the proposed radial DCE-MRI technique is evaluated in subjects with lung and liver lesions, and results demonstrate that excellent pixelwise perfusion maps can be obtained with the proposed methodology.

Keywords

DCE-MRI; respiratory motion; self-gating; autofocusing; principal component analysis

Dynamic contrast-enhanced (DCE)-MRI has emerged as a prime method for evaluating tumor blood flow and capillary wall permeability, which is the target of many emerging antiangiogenic and antivascular agents (1–4). In DCE-MRI, dynamic T_1-weighted image series following the intravenous bolus injection of contrast agents are acquired and subsequently analyzed to characterize tumor micro-vasculature. Accurate perfusion assessment with DCE-MRI requires high temporal resolution, particularly for the arterial

[*]Correspondence to: Wei Lin, Ph.D., Department of Radiology/HUP, 1 Silver-stein/MRI, 3400 Spruce St., Philadelphia, PA 19104., weilin@mail.med.upenn.edu.

input function (AIF). It was previously shown in simulations that the AIF should ideally be sampled every 1–2 s in order to reduce measurement variability in perfusion parameters to less than 10% (5). Sufficient spatial resolution is also needed for the detection of small lesions and assessment of lesion heterogeneity.

DCE-MRI of lesions located in the chest and abdomen (common areas for tumor metastases) is often hindered by respiratory motion artifacts (6,7). To ensure an accurate analysis of tumor-enhancement kinetics, 6–10 min of data must be acquired at a high temporal rate, which requires a free-breathing acquisition. In the presence of respiratory motion, lesion displacement and blurring introduce significant errors into measured perfusion parameters, and make pixel-by-pixel analysis impossible.

Respiratory gating techniques developed for Cartesian acquisitions include the use of pneumatic bellows (8,9) or navigator echoes (10) to monitor the chest wall or diaphragm position. It has been shown that the latter technique provides images with superior quality due to better correspondence with actual respiratory motion (11). For DCE-MRI, however, the need to acquire an additional navigator signal would sacrifice the acquisition efficiency. Instead, an uninterrupted, continuous acquisition of imaging data is preferred in order to achieve the highest possible temporal resolution. Navigator excitations may also undesirably cause regions of low signal in the imaging field of view (FOV).

It has been recognized that radial (projection reconstruction) MRI is suitable for dynamic imaging because a high temporal resolution can be achieved by acquiring azimuthally undersampled data sets (12–14). At the same time, radial imaging provides unique opportunities for motion compensation. Since the central *k*-space region is repetitively sampled, certain data consistency constraints can be applied to reduce motion artifacts (15). It also becomes possible to estimate and compensate for motion by comparing undersampled images acquired at different time points (16). Recently, Larson et al. (17) proposed to extract several self-gating signals, including echo magnitude, center of mass, and image correlation values, for breath-held 2D cardiac cine MRI. These gating signals were used to guide the retrospective reconstruction of images at different cardiac phases. The method was later extended to free-breathing 2D cine MRI (18), where image correlation between an undersampled data set and a low-resolution reference is performed in real time. This procedure requires repeated acquisition of an undersampled image until acquisition at end-expiration is ensured.

Recently, a golden-angle view-ordering scheme with a high degree of reconstruction flexibility was proposed for radial imaging (19). In this scheme, a single special “golden angle,” given by $\theta_G = (\sqrt{5}-1)/2 * 180^\circ \approx 111.246^\circ$, is used to increment successive view angles. The desirable feature of this scheme is that the azimuthal sampling is approximately uniform for an arbitrary number of consecutive views at an arbitrary temporal position. Such flexibility is particularly attractive for free-breathing imaging applications because it becomes possible to reconstruct an image series where each image is centered at temporal positions with minimal motion, such as end-expiration. Furthermore, it allows the number of views used to reconstruct each image to be determined retrospectively, precluding the need for a priori knowledge of the respiratory rate, which can vary during the scan session. In

addition, the golden-angle radial acquisition has an intrinsic motion-reduction property due to pseudo-random angular increments between successive views, similar to a segment permutation strategy described previously (20).

The purpose of this work is to develop and evaluate a robust radial DCE-MRI technique capable of acquiring high-quality images and accurate perfusion maps in regions where standard methodologies fail due to respiratory motion. These goals are accomplished by incorporating various motion-compensation and image enhancement strategies: 1) radial self-gating for respiratory motion compensation; 2) autofocusing and image correlation to further enhance image sharpness; and 3) *k*-space-weighted image contrast (KWIC) filtering and principal component analysis (PCA) to reduce image streaking and enhance the signal-to-noise ratio (SNR) of the dynamic series. The performance of the proposed technique is evaluated in subjects with lung and liver lesions.

MATERIALS AND METHODS

Respiratory Self-Gated DCE-MRI

The proposed DCE-MRI method is summarized in Fig. 1. A 3D golden-angle hybrid radial acquisition scheme was modified from a conventional spoiled gradient-echo sequence. The inner slice-encoding loop is phase-encoded, while in-plane a golden-angle radial acquisition scheme is used (19) in which a fixed angular offset of $\theta \approx 111.25°$ advances successive view angles throughout the free-breathing DCE-MRI scan. Following data acquisition, the peak echo magnitude at $k_z = 0$ is processed to generate a respiratory self-gating signal (Fig. 2). This signal represents the total transverse magnetization within the coil sensitivity region. It is sampled once every N*TR, where N is the number of slice encodings. For this study, TR = 3.2 ms and the number of slice encodings N = 13 (for partial k_z acquisition of 16 slices); therefore, N*TR = 42 ms. In a multicoil setup for imaging the chest or abdominal region, a single anterior or posterior coil positioned near the diaphragm is chosen because the changes in the peak signal are expected to be the greatest in this region (21). Since the views are incremented by a large angle (golden angle, 111.25°), the peak signal can change rapidly due to factors unrelated to respiration, including those caused by field inhomogeneity, eddy currents, and/or imperfect *k*-space trajectory (22). Thus, a low-pass filter is first applied to remove the unwanted signal fluctuations. The lower curve in Fig. 2 is the low-pass filtered signal from a DCE-MRI scan, showing both a fast-changing periodic component due to respiratory motion and a slowly increasing average signal due to the contrast arrival. To detect the peak end-expiratory positions (local signal maximum), a high-pass filter is further applied to remove the slow component, resulting in a band-pass filtered signal (upper curve in Fig. 2). Then a local maximum search is performed to determine the end-expiration positions.

Following the detection of end-expiratory positions, consecutive views within each respiratory cycle are grouped into a segment for reconstruction. In a golden-angle radial data set, an approximate azimuthal uniformity is achieved for an arbitrary number of views centered at an arbitrary time point, although optimal uniformity is achieved when the number of the views is a member of the Fibonacci series (19):

$$F(k)=\{1,1,2,3,5,8,13,21,34,55\ldots\}, F(k+2)=F(k+1)+F(k),\ k\geq 0. \quad [1]$$

As a result, depending on the respiratory period of individual patients, segments with 34 or 55 views were used in this work, corresponding to a temporal window of 1.4–2.3 s. As will be demonstrated, data acquired during end-expiration exhibit the least amount of both intra- and intersegment lesion motion. In this work, we therefore propose to use only end-expiratory segments for our proposed technique, as the rigid-body motion assumption is mostly likely to hold true for this respiratory phase.

For the reconstruction of each segment, an inverse Fourier transform is first taken along k_z to separate the slices, prior to 2D regridding of each slice using a Kaiser-Bessel kernel width of four points (23). Data from different coils are reconstructed separately prior to a modified form of sum-of-squares combination, where coil sensitivities are estimated from low-resolution images to reduce interference from streaking artifacts (24). The result of this self-gating procedure is an undersampled, respiratory-gated, dynamic image series.

Intrasegment Motion Compensation

Although the end-expiratory period is expected to be relatively free of motion, a small amount of intrasegment motion may occur, particularly at the beginning and end of each segment. To further compensate for motion that may occur within each segment, a regional autofocusing correction method was developed for radial imaging. Originally proposed for Cartesian acquisitions (25), autofocusing is a postprocessing technique that optimizes an image quality metric while different trial corrections are applied to the motion-corrupted data. Although the overall chest and abdominal regions generally undergo nonrigid deformation during respiration, for small displacements of the lesion occurring within each segment, correction for rigid-body translation may be sufficient. Thus, in this work, the 3D rigid-body intrasegment lesion translation is compensated for by minimizing the image entropy computed over a rectangular region of interest (ROI) encompassing the lesion. For Cartesian acquisitions, it has been found that several image gradient-based metrics, such as gradient entropy and normalized gradient squared, give superior performance (26). However, we have found that gradient-based metrics are less robust for radial imaging and favor images with more streaks. In contrast, entropy was found to be suitable for radial autofocusing. The regional entropy is defined by:

$$E=-\sum_{i\in R}[(B_i/B_0)\ln(B_i/B_0)], \quad B_0=\sqrt{\sum_{i\in R}B_i^2}. \quad [2]$$

Here R is the ROI, B_i is the pixel intensity at the coordinate i within the ROI, and B_0 is used to gauge the total image energy in this region. A fifth-order polynomial function was used to model smooth respiratory motion within each segment. The ranges of motion were limited to physiologically reasonable values (±5 cm along the superior/inferior [S/I] direction, and ±1 cm along the left/right [L/R] and anterior/posterior [A/P] directions). After linear phases introduced by 3D trial motion were applied to the acquired data segment, images were

reconstructed and regional entropy was minimized against motion model parameters using the Nelder-Mead (simplex) nonlinear optimization algorithm (27). Following motion estimation, appropriate phase corrections were applied to each view to compensate for the intrasegment motion.

Intersegment Motion Compensation

Since the position of a lesion can vary between different respiratory cycles, intersegment translational motion compensation was also performed. Following intrasegment motion compensation, each segment image was aligned with a reference image by maximizing a regional 3D image cross-correlation function (28,29). An end-expiratory segment with the smallest image entropy value (and therefore the best image quality) was used as the reference and the ROI previously selected for autofocusing was used. The normalized regional image cross-correlation function between the reference image *I* and target image *J* on the ROI *R* is defined as:

$$C_{i,j}^{R}(\Delta r)=\frac{\sum_{r\in R} I(\mathbf{r})J(\mathbf{r}+\Delta\mathbf{r})}{\sqrt{\sum_{r\in R} I^2(\mathbf{r})}\cdot\sqrt{\sum_{r\in R} J^2(\mathbf{r}+\Delta\mathbf{r})}}=\frac{(m\cdot l)\otimes J}{\sqrt{\sum_{i\in R} I_i^2}\cdot\sqrt{m\otimes(J\cdot J)}}. \quad [3]$$

Here Δ*r* is the translation vector, *r* is the image voxel coordinate, ⊗ denotes convolution, and *m* is a mask image with pixel values of one in the predefined ROI and zero elsewhere.

Once $C_{I,J}^{R}$ is computed, the relative 3D translation of image *J* with respect to the reference image *I* can be determined from the Δ*r* with the maximal correlation value. The two convolutions in Eq. [3] can be computed rapidly through data multiplication in *k*-space, since convolution in image space corresponds to multiplication in *k*-space. To achieve subpixel motion detection, the *k*-space data were first zero-filled prior to multiplication, resulting in an isotropic resolution of 1 mm in all three spatial dimensions. The size of the mask image was chosen to ensure the detection of all possible lesion motion within a physiologically reasonable range, while minimizing the computational cost. Following the detection of intersegment translation, appropriate linear phases were applied to each view to compensate for the shifts.

KWIC/PCA Processing

The result of the above motion correction procedures is an undersampled series of respiratory-motion compensated images, with a temporal resolution equal to the respiratory period. Since each end-expiratory image consists of only 34–55 radial views and each readout line has 192 data points, considerable level of streaking artifacts may appear due to the violation of the Nyquist criterion in the outer *k*-space regions. Furthermore, because of the small number of views used for each image, SNR may also be reduced. To address these two issues, we investigated two methods to reduce streaking and enhance SNR: KWIC and PCA.

The KWIC technique was previously proposed to achieve simultaneously high temporal and spatial resolution for dynamic radial imaging (14,30), based on the observation that image contrast is predominantly determined by the data near the *k*-space center. In this work, the KWIC technique is adapted for noncontiguous data sets from different end-expiratory segments. As shown in Fig. 3, *k*-space is first divided into concentric rings. The central *k*-space circle contains data from only the current segment 0, while the adjacent annular region (bounded by the next larger circle) contains additional data from the two adjacent respiratory cycles (segments −1 and 1). Further out, data from two more adjacent respiratory cycles are also included (segments −2 and 2), and this process continues until data from seven to nine total segments are included in the outermost *k*-space region, depending on the number of views per segment. The boundary of each circular region is determined by the Nyquist criterion, assuming for the sake of simplicity that the views within each region have uniform azimuthal spacing. Although the views within each ring are not consecutively acquired, the pseudo-random property of golden-angle view-angle ordering typically results in a good azimuthal distribution. Local sampling-density compensation weighting was applied prior to the standard 2D regridding.

We also investigated the PCA technique to enhance image SNR and reduce streaking. PCA is a technique that can be used to statistically analyze image series, separating them into an orthogonal set of temporal response functions (component vectors) and their corresponding component images (weighting functions). Specific components contributing mostly to noise or undesired artifacts such as streaking could subsequently be excluded, while the desired components are retained. The utilization of PCA in a dynamic PR image series was previously reported to remove subtle streaking artifacts (31), as well as more substantial ones in highly undersampled dynamic series (32). In the current implementation, a singular value decomposition (SVD) was performed on the magnitude of the undersampled dynamic image series. The resulting eigenvectors yield temporal response component vectors, while the projections onto these vectors give corresponding component images. Both component images and time series were then visually inspected to exclude those corresponding to streaks and noise. The remaining components were combined to obtain the PCA-processed dynamic image series.

AIF Sampling

The AIF is required in order to perform perfusion analysis using the two-compartment exchange model (1). Since the AIF can vary significantly between different subjects (or within the same subject at scan sessions) (33,34), it is ideal to measure the true AIF rather than use an assumed function as is often done. In our DCE-MRI scans, the aorta is included in the imaging volume, allowing the patient-specific AIF to be measured. Since respiratory motion is negligible in the aorta, no motion compensation is necessary, permitting the utilization of an ungated, continuous data set. To obtain a high-temporal-resolution AIF function, a sliding-window reconstruction was carried out using 34-view segments resulting in an effective sampling rate of 1.4 s, with an intersegment shift of 24 views. Since the AIF is derived from the mean of many voxels in the aorta, it was found that subsequent KWIC/PCA processing is not necessary to derive an accurate AIF curve.

T_1 Mapping

The baseline T_1 value of the lesion prior to contrast injection is needed to convert the DCE-MRI image intensities into contrast agent concentration for subsequent perfusion analysis. Traditionally, T_1 measurements are often carried out during breath-holding to avoid respiratory motion artifacts. However, in high-resolution or large-volume 3D imaging, scan times can become prohibitive. Further, prolonged breath-holding can be difficult for some patients, particularly those with lesions in the lung.

In this work, we utilize a dual flip-angle radial T_1 mapping procedure based on the free-breathing golden-angle acquisition scheme similar to that proposed for radial DCE-MRI (35). Each of the two scans lasts 1.5 min and is run prior to the DCE-MRI exam. Two flip angles ($\alpha = 3°, 10°$) were selected to minimize the T_1 measurement error at TR = 3.2 ms, assuming a nominal lesion T_1 value of 650 ms (36,37). Following respiratory self-gating, end-expiratory segments from all respiratory cycles (except the first to ensure steady state) are combined to reconstruct a single image for each flip angle. The signal intensity ratio of two motion-compensated images is then used to compute a T_1 map (38).

Scan Protocol

To evaluate the efficacy of our technique, five patients with metastatic lesions in either the lung or the liver were scanned for a total of six exams (one patient was scanned at two different time points). In first four exams, radial DCE-MRI was performed following a standard Cartesian protocol in the same scan session (with the second injection occurring about 10–15 min after the first injection), allowing the comparison of the image qualities. In the remaining two exams, only radial DCE-MRI was performed. The study was approved by the institutional review board and all subjects gave informed consent. Imaging was performed on a 1.5-T Siemens Sonata scanner using anterior torso and a posterior spine coil arrays. Contrast agent (0.1 mmol/kg of gadodiamide: Gd-DTPA-BMA; Ominscan, Nycomed, Norway) was administered 15 s into the dynamic scans, using an infusion pump that was synchronized with the scanner, followed by a 20-ml saline flush. 3D oblique coronal imaging volumes (typically $380 \times 380 \times 80$ mm^3) were selected by an experienced radiologist to provide the maximum coverage for the tumor(s), as well as the aorta to provide AIF sampling.

In the standard Cartesian protocol, the dynamic scan was conducted using a 3D fast low-angle shot (3D FLASH) sequence. Radial DCE-MRI was performed using the proposed 3D hybrid radial sequence with similar imaging parameters as the Cartesian protocol: flip angle $\alpha = 30°$; matrix size (radial) = 192 (readout) × 4000 – 8000 (total views); matrix size (Cartesian) = 256 (readout) × 128 (phase encodes per image), resulting in 1:2 pixel dimension; 16 slices; TR/TE = 3.2/1.5 ms; total scan time = 3–7 min. Partial Fourier encoding was performed along the slice direction, where the 16 slices were reconstructed from 13 phase-encoding steps after zero-filling in *k*-space. In our first subject (with lung tumor), the proposed T_1 mapping scheme was not performed, and instead a T_1 map acquired after a Cartesian-only DCE-MRI protocol in a follow-up visit was used. In the remaining subjects with the liver tumor, free-breathing radial T_1 mapping was performed prior to the radial DCE-MRI scan using two 1.5-min acquisitions (2000 views each) with flip angles $\alpha =$

3°, 10°. The patients were asked to breathe normally throughout both the radial T_1 mapping and both dynamic series. For the radial scans, raw data were transferred offline for subsequent processing, while standard online reconstructions were performed for Cartesian scans.

To evaluate the effectiveness of the proposed respiratory motion compensation strategy on all data sets, regional image entropy values were compared over the lesion ROI using radial data sets only. For this purpose, postcontrast images reconstructed with self-gating and intra- and inter-segment motion correction (combination of 10 end-expiratory segments of 55 or 34 views depending on the respiratory cycle, without PCA or KWIC processing) were compared with those reconstructed without the motion-compensation steps (550 or 340 contiguous views).

Following processing of the dynamic series with the proposed methodologies, the volume transfer coefficient K^{trans}, extracellular extravascular volume fraction v_e, and plasma volume fraction v_p were determined in the tumor region by a pixel-by-pixel fitting of the contrast concentration in the tumor, C_t, based on the following equation (3):

$$C_t(t)=v_P C_P(t)+K^{trans}\int_0^t C_P(t')\exp[K^{trans}(t-t')/v_e]dt'. \quad [4]$$

Here $C_p(t)$ is the concentration of the contrast agent in plasma, derived from the AIF. The fitting was performed using a simplex nonlinear optimization algorithm (27) and required less than 1 min for a lesion with 1000 voxels. Temporal points for the lesion signal (C_t) used for performing Tofts model fitting have irregular intervals, since they correspond to the midpoints of contiguous end-expiratory segments. Therefore, the fitting term on the right-hand side of Eq. [4], which is derived from high-temporal-resolution AIF data (C_p), was linearly interpolated onto the irregular lesion signal time points prior to the error minimization.

RESULTS

Respiratory Motion Compensation

The proposed self-gating method successfully detected respiratory motion in all six patient exams. The self-gating signal contains a high degree of variation in terms of both periodicity and amplitude. For the patient data shown in Fig. 2, the minimum and maximum respiratory cycle lengths were 3.3 and 6.7 s (average was 4.2 s), respectively, during the 3.5-min acquisition window. This highlights the benefits of using the golden-angle acquisition scheme, which allows the flexibility to center each image at an arbitrary time point.

In order to quantify the lesion displacements that occur during the exam, a continuous (ungated) series of images were created from the radial DCE-MRI data set using sliding-window reconstruction of 55 views per image and a shift of 10 views between adjacent images. Each image was corrected for intrasegment motion using the autofocusing procedure and was subsequently correlated with an end-expiratory reference image to detect 3D lesion displacements. Figure 4a and b show the detected displacements for a lung lesion

and a liver lesion. It can be seen that lesion motion is most significant along the superior/inferior (S/I) direction. The maximum S/I displacements relative to end-expiration, occurring at end-inspiration, ranged from 15 to 20 mm (mean = 17.8 mm) for the lung lesion, and from 3 to 10 mm (mean = 7.0 mm) for the liver lesion. Displacements along the other two directions were found to be much less (≤3 mm). Two further observations can be made. First, the peak expiratory position detected from self-gating signal (marked by open diamonds) is highly consistent throughout the scan, while end-inspiratory positions (valleys) are more variable, reflected by different depths of the valleys at different respiratory cycles. Even for the lung lesion, the maximum deviation of the peak expiratory position was found to be no more than 2 mm along all three directions during the entire 3.5-min DCE-MRI study. The second observation is that there is a relatively long period of "plateau" around each end-expiratory peak indicating negligible motion, particularly for the lung lesion. Both of these two factors contribute to the superior quality of end-expiratory images, as will be shown next.

Figure 5 shows results from the respiratory self-gating, intra- and intersegment motion-compensation procedure for a lung lesion patient. Lesion displacements within each 55-view segment detected from autofocusing are shown in Fig. 5a and b, for end-expiratory and end-inspiratory segments, respectively. Segments from all 38 respiratory cycles during the entire radial DCE-MRI scan are shown. Although variations could be observed between respiratory cycles, the overall shape of the motion trajectories is consistent with the expectation that lesion position is highest (most superior) at end-expiration and lowest (most inferior) at end-inspiration. More significant motion tends to occur near both ends of the 55-view segments (which span 2.3 s). The range of intrasegment motion is smaller at end-expiration than at end-inspiration (notice the scale difference between the two plots). Figure 5c and d show the self-gated radial DCE-MRI images of a lung lesion at end-expiratory and end-inspiratory phases. Each image was reconstructed by combining 55-view segments from 10 consecutive respiratory cycles (for a total of 550 views per image). End-expiratory phase images (Fig. 5c) use only those segments centered at end-expiration peaks detected from the self-gating signal, while end-inspiratory images (Fig. 5d) utilize data shifted by half of the respiratory period. It can be seen that the end-expiratory phase yields a better image quality, while the end-inspiratory image is significantly degraded by respiratory motion. Nonmoving tissues (e.g., the spine and aorta), however, remain mostly motion-free during all respiratory phases. It is also readily apparent from the images that motion induces only local displacements and blurring (as opposed to more distant ghosting effects) with the golden-angle radial scheme, justifying the proposed regional motion-compensation methods. Figure 5e and f further show images at end-expiration and end-inspiration after both intra-and intersegment motion compensation. Significant improvements in image quality can be observed at end-inspiration due to the greater extent of both intra- and intersegment lesion displacements, while improvements for end-expiratory images are more subtle.

Figure 6 compares the radial DCE-MRI images, both without and with the proposed motion-correction methods (including self-gating, intra- and intersegment motion compensation), with those from the conventional Cartesian acquisition for a lung tumor patient and a liver tumor patient. Although the Cartesian images have reduced resolution along the L/R direction due to the anisotropic matrix size (256 × 128 vs. 192 × 192 for radial), the two

acquisition schemes have similar FOVs and slice thicknesses, and therefore a similar voxel size. In these exams, since radial DCE-MRI was performed following the standard Cartesian protocol, residual contrast agent could account for the contrast difference between the radial and Cartesian images. In addition, radial images were often reconstructed with data from one or more coils excluded to further suppress streaking. Free-breathing Cartesian images (Fig. 6a and d) and radial images reconstructed from consecutive views (Fig. 6b and e) show significant blurring of both lesions as well as the lung/liver boundary. On the other hand, radial images with motion-compensation clearly delineate both the lesion boundaries and the lung/liver interface (Fig. 6c and f). The entire motion compensation process took less than 10 min for the end-expiratory segments from the entire radial DCE-MRI data set. When comparing radial images before and after motion compensation, the changes in image entropy computed over the lesion ROIs were −3.9% and −1.4% for the lung patient and the liver patient, respectively.

Figure 7 shows results from three other patients, comparing postcontrast radial DCE-MRI images without and with the proposed motion-correction method. It can be seen that lesion blurring was significantly reduced with the proposed method in all subjects, with the entropy values changed by −0.6%, −0.9%, and −6.2%. In summary, when compared with images without motion compensation, motion-compensated images yield lower entropy values in all six exams, corresponding to sharper images. The average change in entropy after self-gating was −2.4% with a range of −0.6% to −6.2%.

T_1 mapping

Figure 8 shows images from the T_1 mapping procedures for a liver patient. Figure 8a and b compare the ungated and self-gated images, showing a significant reduction of blurring in the lesions using the proposed self-gating method. Figure 8c shows the computed T_1 map, where the peripheral regions of the tumors have lower T_1 values than the core areas. Since in our current experimental protocol, T_1 mapping was carried out following the Cartesian DCE-MRI exam, our measured T_1 values will be lower than the native T_1 value due to the residual contrast agent in the tissue.

PCA and KWIC Processing

Figure 9 demonstrates the PCA processing on the lung patient data, showing the component images (Fig. 9a) and the corresponding temporal functions (Fig. 9b) for the first five components with the highest eigenvalues in descending order. It can be seen that the first three components separate the dynamic data into time series with different spatial contrasts corresponding to various tissues. In contrast, component images 4 and 5 are dominated by streaks with little information in the lesion or the aorta. The corresponding time series also shows no correspondence with the contrast injection (around frame 10), but rather reflects the pseudo-random azimuthal sampling of golden-angle view-ordering scheme. Components 6–38 also showed predominantly noise and streaking artifacts. These observations permit the inclusion of only the first three principal components and exclusion of others to obtain images with reduced streaks and improved SNR.

Figure 10 shows the results of KWIC and PCA processing on the undersampled dynamic radial data sets. The images demonstrate that both KWIC and PCA can effectively reduce image streaking and enhance the SNR of the undersampled data sets. More importantly, these improvements were achieved while preserving high spatial resolution and maintaining the effective temporal resolution.

Perfusion Analysis

Figure 11 shows results from the perfusion analysis of two lung and liver lesions using PCA processing. For the AIF curves (Fig. 11a and d), the sampling rate of 1.4 s per data point is sufficient to sample the fast signal-changing period during the initial contrast arrival. The slower-enhancing tumor curves are also sufficiently sampled with our strategy, where the frame rate equals the respiratory rate. The K^{trans} and v_e maps computed after perfusion model fitting demonstrate that pixel-by-pixel mapping is feasible with our proposed methodology. With such pixelwise analyses, tumoral heterogeneity can be observed. Such high-resolution perfusion parameter maps cannot be obtained using the conventional free-breathing Cartesian technique due to respiratory motion. The computed K^{trans} and v_e values are within ranges reported earlier (3).

Both PCA and KWIC processing significantly reduced the fitting error for the subsequent pixel-by-pixel perfusion analysis. For the data shown in Fig. 10a–c, the RMS fitting error for the contrast agent concentration in the lesion pixels to the model was reduced by 61% and 74% from the undersampled data set after KWIC and PCA processing, respectively. Similar error reduction ratios were also observed for the liver lesion. The average perfusion values generated with KWIC and PCA processing are in good agreement. For the lung lesion, the mean K^{trans} values were 0.233 and 0.231 min^{-1} using PCA and KWIC processing, respectively. The mean v_e values were 0.251 and 0.294 using PCA and KWIC processing, respectively. The mean v_p values were 0.015 and 0.016 using PCA and KWIC processing, respectively.

DISCUSSION

The proposed golden-angle radial acquisition scheme is exceptionally well suited for free-breathing DCE-MRI due to several considerations. First, echo magnitude data provided by the radial acquisition provides a gating signal that allows robust respiratory self-gating without the need for additional navigators. Second, due to the pseudo-random nature of the view angles, the reconstruction window for each image can be positioned at a position where motion is minimal (end-expiration), and the number of views used for reconstruction of each segment can be chosen retrospectively. At the same time, good angular distributions of view angles are always achieved. Further, unlike previous retrospectively gating methods, the periodicity of motion does not have to be estimated a priori.

The utilization of KWIC and PCA processing techniques significantly reduces image streaking and noise while maintaining the spatial and temporal resolution of the undersampled series. Although the relative performance and accuracy of the two methods require further investigation, it is worth noting their respective advantages and disadvantages. KWIC is able to reduce streaking artifacts by avoiding azimuthal

undersampling in *k*-space, by combining data acquired from neighboring segments in the outer *k*-space regions. Image SNR is also increased due to the use of more data. However, the larger temporal window in the outer *k*-space regions causes averaging of high-spatial-frequency data. As a result, the temporal profile of pixels near the edges of lesions may be less accurate, particularly during the initial contrast arrival period, when the signal is rapidly changing. However, it was previously shown that with "undersampled KWIC," where the radii of the circular regions shown in Fig. 3 are increased, more accurate temporal response could achieved even for small objects (5 pixels wide) (14), although at a cost of slightly increased image streaking and reduced SNR.

PCA processing, on the other hand, does not explicitly combine data from different segments, and as a result, a more genuine temporal profile may be possible to achieve. It was previously shown through simulation that PCA processing was able to derive accurate perfusion parameters and reduce error in the computed perfusion parameters when compared with undersampled data sets (32). A potential problem with PCA lies in the uncertainty associated with the component selection process. If too many components are included, the ability to remove streaking artifacts and noise will be compromised. On the other hand, selecting too few components may alter the true enhancing behavior of the lesion and the AIF. In this initial work, we chose to select PCA components visually from the component images and time series. Further investigation is required to determine the optimal trade-off between streaks/noise reduction and the need to maintain the fidelity of temporal profile. It may also be beneficial to perform local PCA processing in a smaller region surrounding each lesion in order to minimize possible interference from other tissue with different enhancing behavior.

In clinical practice, larger imaging volume (more slices) may be desired to assess whole-organ or multi-organ tumor burden. With conventional techniques, this would entail reduced temporal resolution for both the AIF and the tumor. However, in our proposed method, the frame rate is determined by the respiratory period, independently of the number of slices. Instead, greater number of slices entails fewer view angles will be acquired during each respiratory cycle. One of two things could then be considered during reconstruction: First, fewer views could be used for each segment if it is desirable to utilize data from the same fraction of the respiratory cycle as before. This may lead to increased streaking artifacts, and if the methods described in this work are not sufficient for removing these artifacts, additional means to reduce the streaking may be worth exploring (39,40). Second, data from a larger fraction of the respiratory cycle could be used. This may introduce greater intrasegment motion, but our results in Fig. 5 suggest that it should be possible to compensate for the increased motion with our proposed intrasegment motion compensation strategy.

In this work, only 3D rigid-body translation of the lesion was considered. For end-expiratory segments, this assumption holds well due to the limited amount of motion, both within each segment and between segments acquired at different respiratory cycles. In some cases, it may be desirable to include data from other respiratory phases as well, as this will further increase the temporal resolution of the lesion signal. Including both end-expiratory and end-inspiratory segments, for example, will increase the temporal resolution by a factor of 2.

Including data from different respiratory phases in the voxel-based perfusion analysis, however, may require the correction of other types of motion, such as rotation and/or non-rigid deformation. Rotational motion correction using both autofocusing (41,42) and the correlation measure (28,29) has been previously demonstrated and may be adapted for radial acquisition. It may also be possible to extend the non-rigid motion correction technique previously developed for Cartesian imaging (43) to radial imaging.

For the intersegment motion correction using cross-correlation, a postcontrast image was used as the reference. This was found to be effective in the six cases we investigated, and no significant motion estimation error was observed during the DCE-MRI acquisition period. However, the method may not be as successful in some cases, e.g., when the relative contrast between a lesion and its background reverses during contrast enhancement. One possible improvement to the cross-correlation strategy would be to use a moving reference to account for the changes in contrast. Another possible approach is an iterative model-based approach (44), where the reference image is modified for each time point, according to the derived perfusion parameters. It is also possible to further register the T_1 map with DCE-MRI images to account for possible bulk patient motion between the two procedures. Because the flip angles used for T_1 mapping and DCE-MRI are different (3° and 10° vs. 30°), one potentially would need to account for the differences in resulting image contrast prior to registration.

The proposed method as implemented in this initial work requires some operator input, and we are currently investigating means to automate some of these steps. For example, in selecting the coil from which to obtain the self-gating signal, the coil with the largest signal magnitude around the respiratory frequency could be automatically selected. For automatic selection of PCA components, spatial features contained in the component images and the frequency content of the component time series potentially could be utilized to select those that contribute to the lesion.

CONCLUSIONS

The challenge facing DCE-MRI in the abdominal and chest region is to overcome respiratory motion while maintaining sufficient spatial and temporal resolution. It is shown in this work that a 3D golden-angle radial acquisition provides unique advantages to meet these needs. Inherent oversampling of the central *k*-space region not only enables high temporal resolution for sampling the AIF, but also provides a self-gating signal for lesion motion compensation. When combined with the reconstruction flexibility provided by golden-angle strategy, a set of end-expiratory images can be generated that contain minimal motion. Residual intrasegment and intersegment tumor motion can be further corrected by radial autofocusing and regional image correlation. Subsequent processing of the motion-compensated undersampled data sets with KWIC or PCA reduces streaking and noise without sacrificing spatial and temporal resolution. The same golden-angle radial acquisition and reconstruction strategy also allows for free-breathing native T_1 mapping. The in vivo patient results presented in this work clearly demonstrate the feasibility of the proposed technique for computing voxel-based perfusion parameter maps in lesions located in regions severely affected by respiratory motion.

References

1. Tofts PS, Kermode AG. Measurement of the blood-brain barrier permeability and leakage space using dynamic MR imaging. 1. Fundamental concepts. Magn Reson Med. 1991; 17:357–367. [PubMed: 2062210]
2. Padhani AR. Dynamic contrast-enhanced MRI in clinical oncology: current status and future directions. J Magn Reson Imaging. 2002; 16:407–422. [PubMed: 12353256]
3. Roberts C, Issa B, Stone A, Jackson A, Wateron JC, Parker GJM. Comparative study into the robustness of compartmental modeling and model-free analysis in DCE-MRI studies. J Magn Reson Imaging. 2006; 23:554–563. [PubMed: 16506143]
4. Barrett T, Brechbiel M, Bernardo M, Choyke PL. MRI of tumor angiogenesis. J Magn Reson Imaging. 2007; 26:235–249. [PubMed: 17623889]
5. Henderson E, Rutt BK, Lee TY. Temporal sampling requirements for the tracer kinetics modeling of breast disease. Magn Reson Imaging. 1998; 16:1057–1073. [PubMed: 9839990]
6. Stevenson JP, Rosen M, Sun W, Gallagher M, Haller DG, Vaughn D, Giantonio B, Zimmer R, Petros WP, Stratford M, Chaplin D, Young SL, Schnall M, O'Dwyer PJ. Phase I trial of the antivascular agent combret-astatin A4 phosphate on a 5-day schedule to patients with cancer: magnetic resonance imaging evidence for altered tumor blood flow. J Clin Oncol. 2003; 21:4428–4438. [PubMed: 14645433]
7. Lankester KJ, Taylor NJ, Stirling JJ, Boxall J, D'Arcy JA, Leach MO, Rustin GJ, Padhani AR. Effects of platinum/taxane based chemotherapy on acute perfusion in human pelvic tumours measured by dynamic MRI. Br J Cancer. 2005; 93:979–985. [PubMed: 16234826]
8. Runge VM, Clanton JA, Partain CL, James AEJ. Respiratory gating in magnetic resonance imaging at 0. 5 Tesla. Radiology. 1984; 151:521–523. [PubMed: 6709928]
9. Bailes D, Gilderdale D, Bydder G, Collins A, Firmin D. Respiratory ordered phase encoding (ROPE): a method for reducing respiratory motion artifacts in MR imaging. J Comput Assist Tomogr. 1985; 9:835–838. [PubMed: 4019854]
10. Korin HW, Ehman RL, Riederer SJ, Felmlee JP, Grimm RC. Respiratory kinematics of the upper abdominal organs: a quantitative study. Magn Reson Med. 1992; 23:172–178. [PubMed: 1531152]
11. McConnell MV, Khasgiwala VC, Savord BJ, Chen MH, Chuang ML, Edelman RR, Manning WJ. Comparison of respiratory suppression methods and navigator locations for MR coronary angiography. AJR Am J Roentgenol. 1997; 168:1369–1975. [PubMed: 9129447]
12. Rasche V, de Boer RW, Holz D, Proksa R. Continuous radial data acquisition for dynamic MRI. Magn Reson Med. 1995; 34:754–761. [PubMed: 8544697]
13. Peters DC, Grist TM, Korosec FR, Holden JE, Block WF, Wedding KL, Carroll TJ, Mistretta CA. Undersampled projection reconstruction applied to MR angiography. Magn Reson Med. 2000; 43:91–101. [PubMed: 10642735]
14. Song HK, Dougherty L. Dynamic MRI with projection reconstruction and KWIC processing for simultaneous high spatial and temporal resolution. Magn Reson Med. 2004; 52:815–824. [PubMed: 15389936]
15. Glover GH, Noll DC. Consistent projection reconstruction (CPR) techniques for MRI. Magn Reson Med. 1993; 29:345–351. [PubMed: 8450743]
16. Schaffter T, Rasche V, Carlsen IC. Motion compensated projection reconstruction. Magn Reson Med. 1999; 41:954–963. [PubMed: 10332879]
17. Larson AC, White RD, Laub G, McVeigh ER, Li D, Simonetti OP. Self-gated cardiac cine MRI. Magn Reson Med. 2004; 51:93–102. [PubMed: 14705049]
18. Larson AC, Kellman P, Arai A, Hirsch GA, McVeigh ER, Li D, Simonetti OP. Preliminary investigation of respiratory self-gating for free-breathing segmented cine MRI. Magn Reson Med. 2005; 53:159–168. [PubMed: 15690515]
19. Winkelmann S, Schaeffter T, Koehler T, Eggers H, Doessel O. An optimal radial profile order based on the golden ratio for time-resolved MRI. IEEE Trans Med Imaging. 2007; 26:68–76. [PubMed: 17243585]
20. Tsao J, Boesiger P, Pruessmann KP. Lattice permutation for reducing motion artifacts in radial and spiral dynamic imaging. Magn Reson Med. 2006; 55:116–125. [PubMed: 16323156]

21. West, JB. Respiratory physiology—the essentials. 5. Baltimore, MD: Lippincott, Williams & Wilkins; 1995.
22. Rasche V, Holz D, Proska R. MR fluoroscopy using projection reconstruction multi-gradient-echo (prMGE) MRI. Magn Reson Med. 1999; 42:324–334. [PubMed: 10440958]
23. O'Sullivan JD. A fast sinc function gridding algorithm for Fourier inversion in computer tomography. IEEE Trans Med Imaging. 1985; 4:200–207. [PubMed: 18243972]
24. Kholmovski, EG.; Parker, DL.; Di Bella, EV. Streak artifact suppression in multi-coil MRI with radial sampling. Proceedings of the 15th Annual Meeting of ISMRM; Berlin, Germany. 2007; p. Abstract 1902
25. Atkinson D, Hill DL, Stoyle PN, Summers PE, Keevil SF. Automatic correction of motion artifacts in magnetic resonance images using an entropy focus criterion. IEEE Trans Med Imaging. 1997; 16:903–910. [PubMed: 9533590]
26. McGee KP, Manduca A, Felmlee JP, Riederer SJ, Ehman RL. Image metric-based correction (autocorrection) of motion effects: analysis of image metrics. J Magn Reson Imaging. 2000; 11:174–181. [PubMed: 10713951]
27. Press, WH.; Teukolsky, SA.; Vetterling, WT.; Flannery, BP. The art of scientific computing. 2. New York: Cambridge University Press; 1992. Numerical recipes in C; p. 408-412.
28. Pipe JG. Motion correction with PROPELLER MRI: application to head motion and free-breathing cardiac imaging. Magn Reson Med. 1999; 42:963–969. [PubMed: 10542356]
29. Lin, W.; Song, HK. 3D EXTRACT (extrapolation and correlation) for rapid correction of 3D rotation and translation. Proceedings of the 14th Annual Meeting of ISMRM; Seattle, WA, USA. 2006; p. Abstract 3204
30. Song HK, Dougherty L. k-Space weighted image contrast (KWIC) for contrast manipulation in projection reconstruction MRI. Magn Reson Med. 2000; 44:825–832. [PubMed: 11108618]
31. Martel, AL.; Ramsay, E.; Plewes, D. Using principal component analysis to reduce the effect of streaking artefacts in dynamic PR-TRICKS images of the breast. Proceedings of the 13th Annual Meeting of ISMRM; Miami Beach, FL, USA. 2005; p. Abstract 1861
32. Guo, J.; Rosen, MA.; Song, HK. Evaluation of principal component analysis for highly undersampled radial DCE-MRI. Proceedings of the 15th Annual Meeting of ISMRM; Berlin, Germany. 2007; p. Abstract 1885
33. Rijpkema M, Kaanders JH, Joosten FB, van der Kogel AJ, Heerschap A. Method for quantitative mapping of dynamic MRI contrast agent uptake in human tumors. J Magn Reson Imaging. 2001; 14:457–463. [PubMed: 11599071]
34. Port RE, Knopp MV, Brix G. Dynamic contrast-enhanced MRI using Gd-DTPA: interindividual variability of the arterial input function and consequences for the assessment of kinetics in tumors. Magn Reson Med. 2001; 45:1030–1038. [PubMed: 11378881]
35. Lin, W.; Song, R.; Rosen, MA.; Song, HK. A free-breathing self-gated 3D golden-angle radial technique for abdominal imaging and T1 mapping. Proceedings of the 15th Annual Meeting of ISMRM; Berlin, Germany. 2007; p. Abstract 1791
36. Denoi SC, Rutt BK, Peters TM. Rapid combined T1 and T2 mappings using gradient recalled acquisition in the steady state. Magn Reson Med. 2003; 49:515–526. [PubMed: 12594755]
37. Fleysher L, Fleysher R, Liu S, Zaaraoui W, Gonen O. Optimizing the precision-per-unit-time of quantative MR metrics: examples for T_1, T_2 and DTI. Magn Reson Med. 2007; 57:380–387. [PubMed: 17260375]
38. Brookes JA, Redpath TW, Gilbert FJ, Murray AD, Staff RT. Accuracy of T_1 measurement in dynamic contrast-enhanced MRI using two and three dimensional variable flip angle fast low-angle shot. J Magn Reson Imaging. 1999; 9:163–171. [PubMed: 10077009]
39. Mistretta CA, Wieben O, Velikina J, Block W, Perry J, Wu Y, Johnson K, Wu Y. Highly constrained backprojection for time-resolved MRI. Magn Reson Med. 2006; 55:30– 40. [PubMed: 16342275]
40. Block KT, Uecker M, Frahm J. Undersampled radial MRI with multiple coils. Iterative image reconstruction using a total variation constraint. Magn Reson Med. 2007; 57:1086–1098. [PubMed: 17534903]

41. McGee KP, Felmlee JP, Jack CR Jr, Manduca A, Riederer SJ, Ehman RL. Autocorrection of three-dimensional time-of-flight MR angiography of the Circle of Willis. AJR Am J Roentgenol. 2001; 176:513–518. [PubMed: 11159106]

42. Lin W, Ladinsky GA, Wehrli FW, Song HK. Image metric-based correction (autofocusing) of motion artifacts in high-resolution trabecular bone imaging. J Magn Reson Imaging. 2007; 26:191–197. [PubMed: 17659555]

43. Batchelor PG, Atkinson D, Irarrazaval P, Hill DL, Hajnal J, Larkman D. Matrix description of general motion correction applied to multishot images. Magn Reson Med. 2005; 54:1273–1280. [PubMed: 16155887]

44. Adluru G, DiBella EVR, Schabel MC. Model-based registration for dynamic cardiac perfusion MRI. J Magn Reson Imaging. 2006; 24:1062–1070. [PubMed: 17031818]

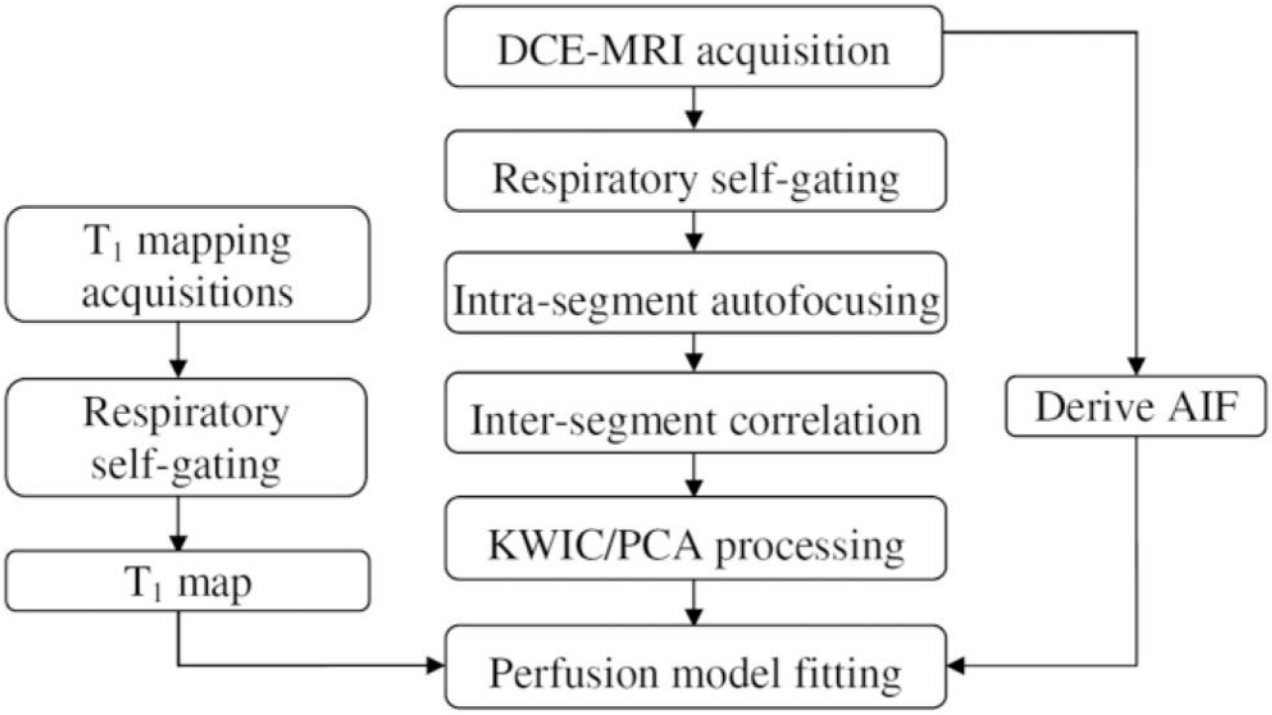

FIG. 1.
The proposed procedure for free-breathing radial DCE-MRI.

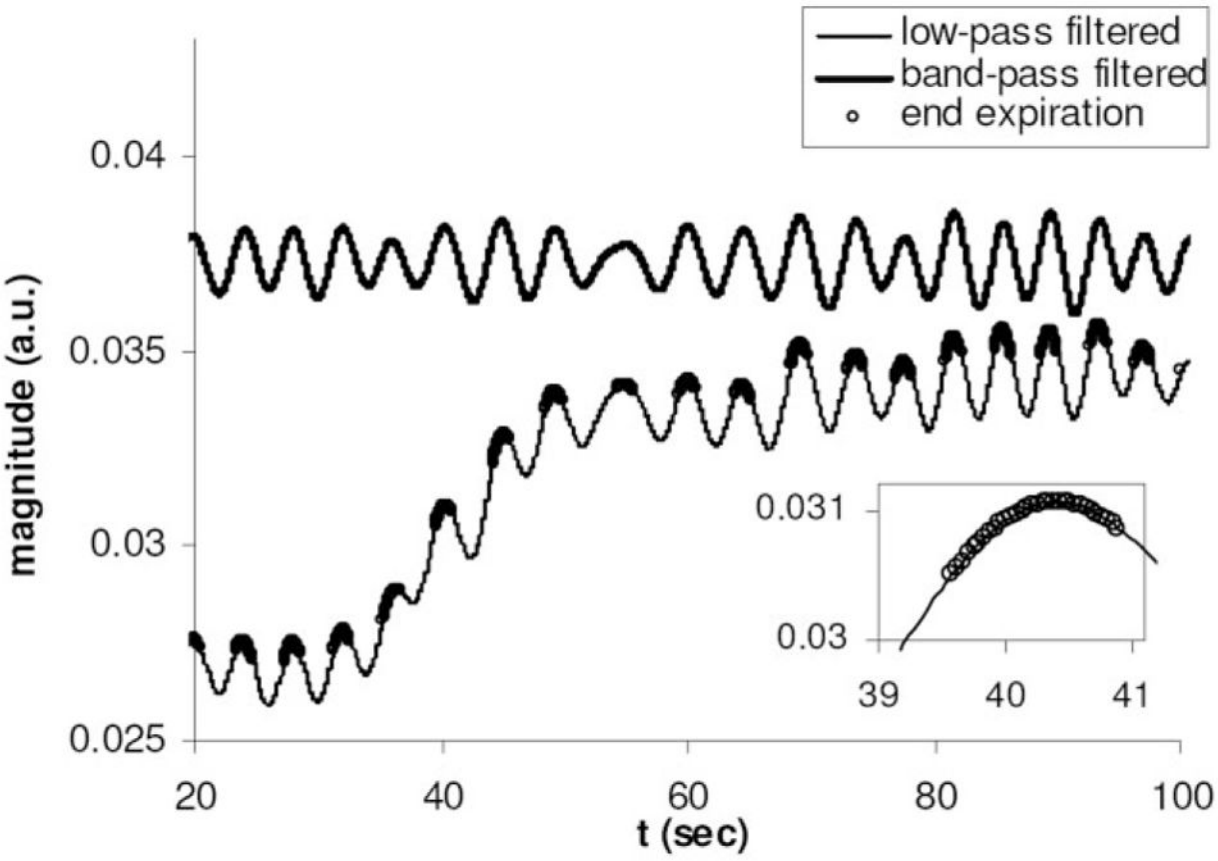

FIG. 2.

The respiratory self-gating signals from a free-breathing radial DCE-MRI scan. The bottom curve is the low-pass filtered signal, which effectively tracks both respiratory motion and signal enhancement following contrast injection. Subsequent application of a high-pass filter results in the upper curve, permitting the detection of the respiratory cycle. Inset shows an end-expiratory segment (open circles) used for subsequent reconstruction.

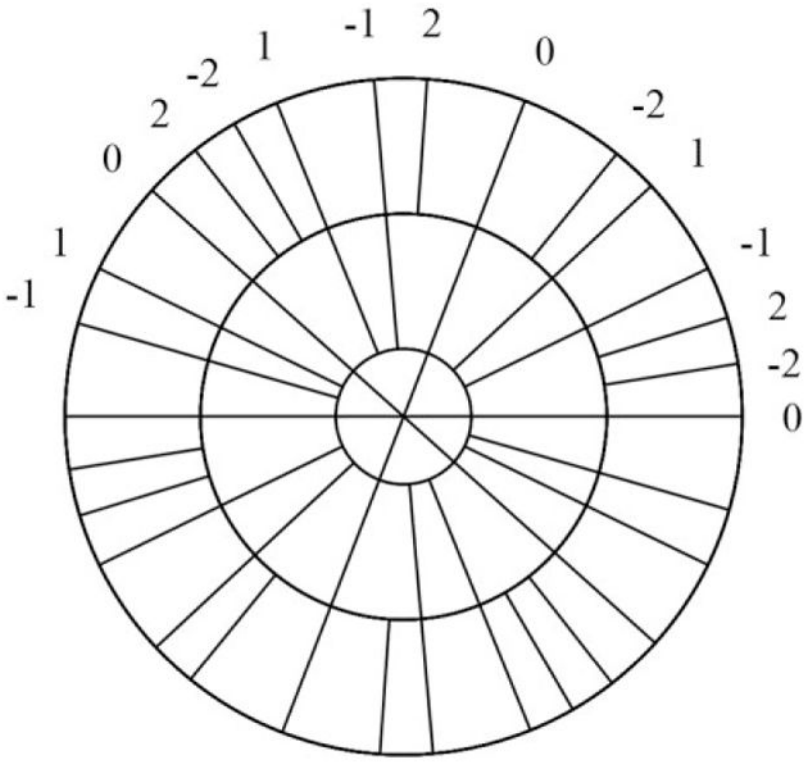

FIG. 3.

Dynamic KWIC processing for the golden-angle radial DCE-MRI acquisition. In the most central *k*-space region, data from only the current segment (0) is used. In the adjacent *k*-space ring, the neighboring two segments acquired before (−1) and after (1) the current respiratory cycle are included. The next ring includes two more neighboring segments (−2 and 2). The radii of the rings are determined from the Nyquist criterion.

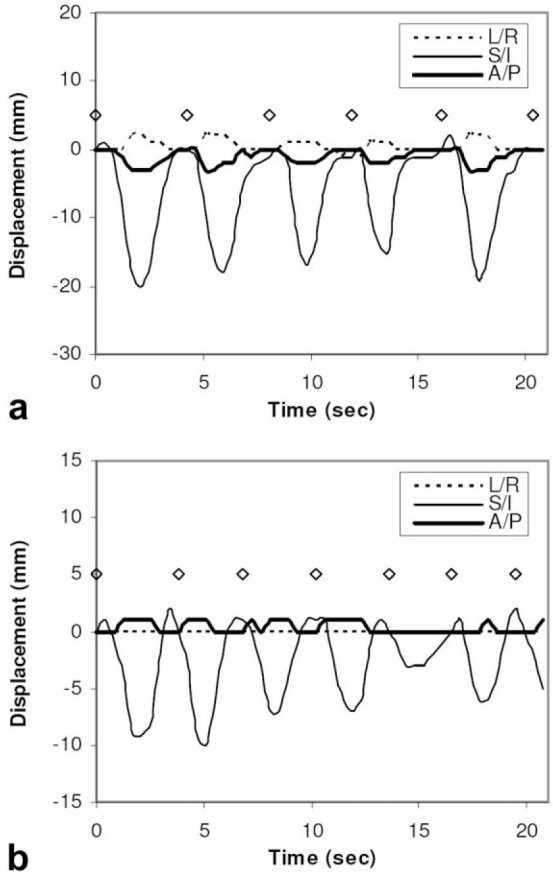

FIG. 4.

Displacement of lesions along the left/right (L/R), superior/inferior (S/I), and anterior/posterior (A/P) directions detected from ungated data sets (**a:** lung lesion; **b:** liver lesion). Peak end-expiratory positions detected from the self-gating signal are also shown (diamonds).

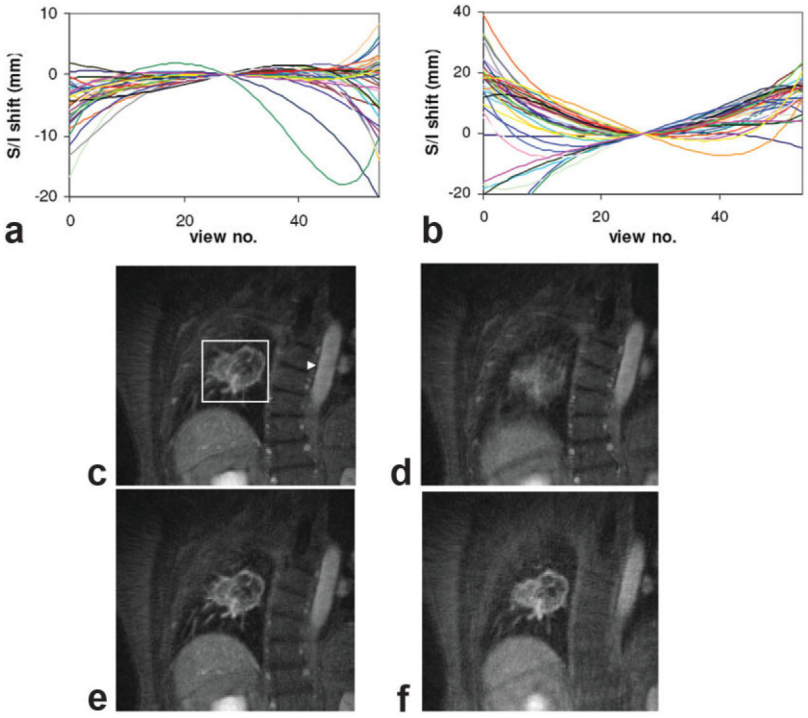

FIG. 5.

Respiratory motion-compensation results from the DCE-MRI study of a lung lesion patient. **a**,**b:** Intrasegment lesion displacement along the S/I direction detected using autofocusing for (a) end-expiratory and (b) end-inspiratory segments, which are centered at the end-expiratory peaks and one-half cycle toward the next end-expiratory peak, respectively. Each segment consists of 55 contiguous radial views, and different lines correspond to segments from different respiratory cycles. The central view of each segment was shifted to position zero so that the general trend within the segments could be easily observed. A positive shift indicates displacement in the superior direction. **c**,**d:** Self-gated end-expiratory (c) and end-inspiratory (d) images after the peak enhancement. Each image was reconstructed by combining 55-view segment data from 10 consecutive respiratory cycles. In c, the arrowhead points to the aorta, while the rectangle is the lesion ROI used for subsequent intra- and intersegment motion compensation. **e**–**f:** End-expiratory (e) and end-inspiratory (f) images following both intra- and intersegment correction. [Color figure can be viewed in the online issue, which is available at http://www.interscience.wiley.com.]

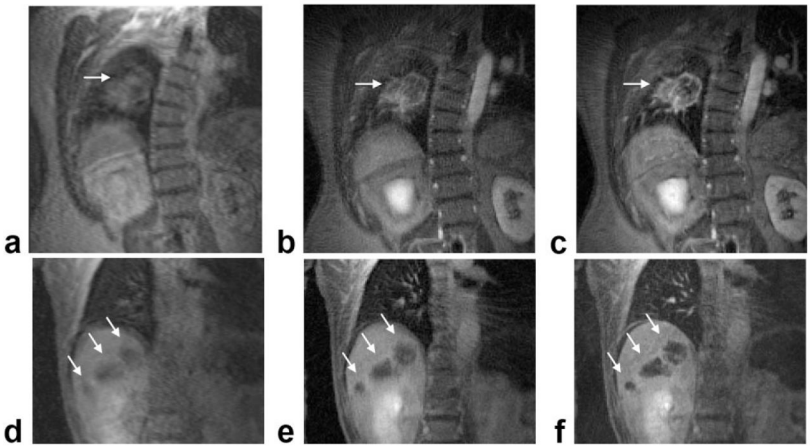

FIG. 6.

Comparison of image quality using the proposed golden-angle radial scheme with conventional Cartesian acquisition. **a:** Cartesian DCE-MRI image of the lung lesion. **b**,**c:** Radial images of the lesion, reconstructed from either 550 consecutive views (b) or from 10 consecutive 55-view motion-compensated end-expiratory segments (c). **d**–**f:** Corresponding images from the liver tumor patient. For this patient, the radial images were reconstructed from either 340 consecutive views (e) or 10 consecutive 34-view end-expiratory segments (f). Lesions are indicated by arrows.

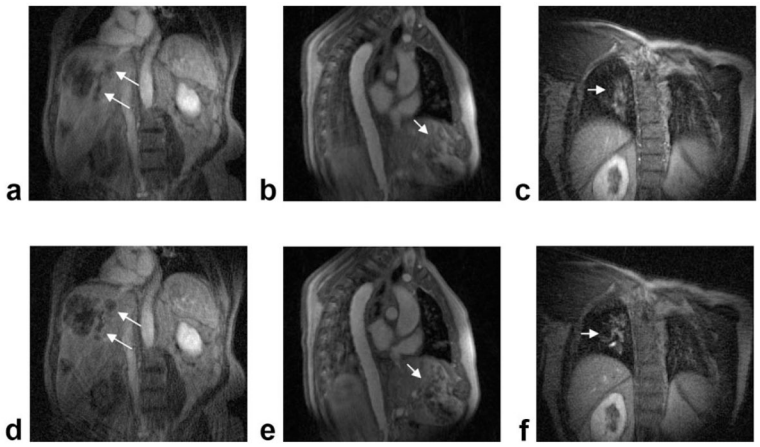

FIG. 7.

Comparison of postcontrast radial DCE-MRI images with and without the proposed motion-compensation strategy. **a–c:** Images reconstructed using 550 or 340 consecutive radial views. **d–f:** Images reconstructed using 10 consecutive motion-compensated end-expiratory segments.

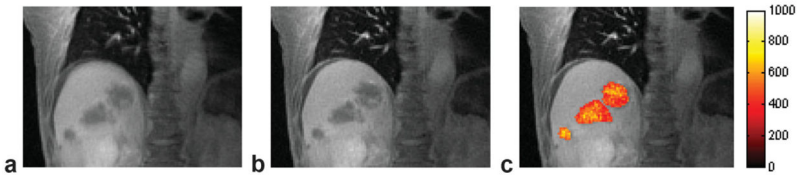

FIG. 8.

Images from the free-breathing T_1 mapping procedure of the liver lesion patient. **a:** Ungated image reconstructed using 850 consecutive radial views. **b:** Self-gated image reconstructed using 850 radial views (25 respiratory cycles, 34 end-expiratory views per segment). **c:** T_1 map in milliseconds.

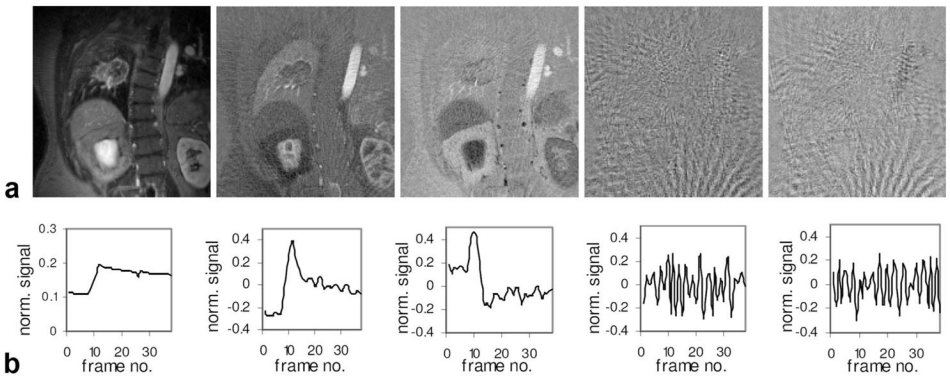

FIG. 9.

PCA processing of dynamic image series for the lung cancer patient. **a:** First five component images. **b:** First five-component time series, showing the normalized signal vs. frame number (respiratory cycle number).

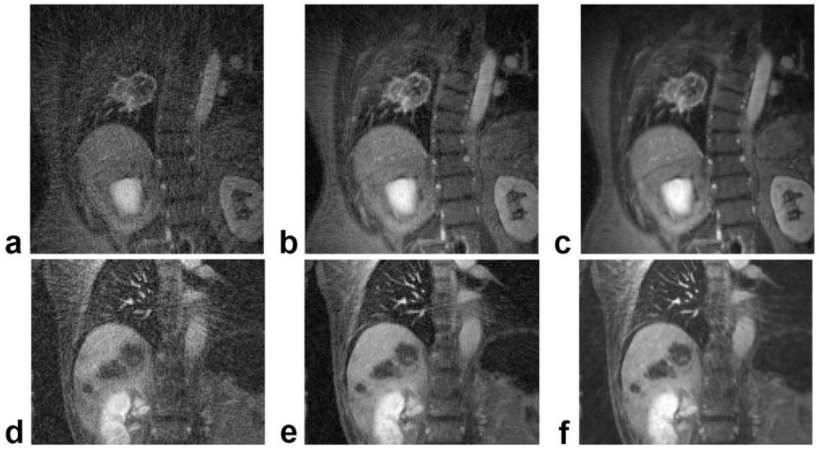

FIG. 10.

KWIC and PCA processing results of the undersampled radial data sets. **a–c:** DCE-MRI images from a lung tumor patient. a: Under-sampled segment image (55 views). b: Dynamic KWIC processed image (seven consecutive end-expiratory segments). c: PCA processed image (using the first three components). **d–f:** Corresponding postcontrast images from a liver tumor patient, using 34-view end-expiratory segments and the first two components for the PCA processed image (f).

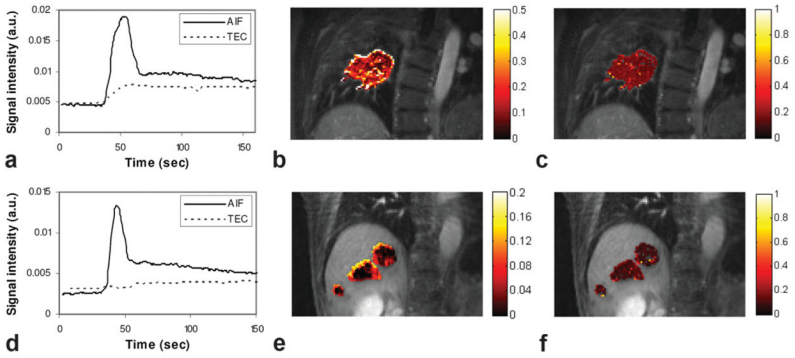

FIG. 11.

Perfusion analysis results: (**a**) the AIF and mean tumor enhancement curve (TEC) for the lung lesion patient; (**b**) K^{trans} map (1/min); (**c**) v_e map. **d–f:** Respective results for the liver tumor patient.